Received: 2 June 2025 | Revised: 25 July 2025 | Accepted: 10 August 2025

DOI: 10.1002/inf2.70073

RESEARCH ARTICLE

WILEY

Exploring the evolution of active sites on Fe_2GeO_4–$Ni_3Ge_2O_5(OH)_4$ interfaces for water oxidation

Tofik Ahmed Shifa[1] | **Karim Harrath**[2] | **Alhagie Jadama**[3] | **Kassa Belay Ibrahim**[1] | **Alessandro Gradone**[4] | **Andrea Migliori**[4] | **Marshet Getaye Sendeku**[5] | **Sandro Zorzi**[6] | **Matteo Bordin**[1] | **Vittorio Morandi**[4] | **Luca Olivi**[7] | **Danilo Oliveira de Souza**[8] | **Alberto Vomiero**[1,5] | **Elisa Moretti**[1]

[1]Department of Molecular Sciences and Nanosystems, Ca' Foscari University of Venice, Venice, Italy

[2]Gan Jiang Innovation Academy, Chinese Academy of Science, Ganzhou, The People's Republic of China

[3]School of Arts and Sciences, Division of Physical and Natural Sciences, Department of Chemistry, The University of The Gambia, Serrekunda, Gambia

[4]Istituto per lo studio dei materiali nanostrutturati (ISMN), Consiglio Nazionale delle Ricerche (CNR), Bologna, Italy

[5]Division of Materials Science, Department of Engineering Sciences and Mathematics, Luleå University of Technology, Luleå, Sweden

[6]Fondazione Bruno Kessler, Center for Sustainable Energy, Povo, Italy

[7]Elettra-Sincrotrone Trieste, Trieste, Italy

[8]Laboratório de Física Médica, Instituto de Física, Universidade do Estado do Rio de Janeiro, Rio de Janeiro, Brazil

Correspondence
Tofik Ahmed Shifa, Kassa Belay Ibrahim, Alberto Vomiero, and Elisa Moretti, Department of Molecular Sciences and Nanosystems, Ca' Foscari University of Venice, Via Torino 155, 30170 Venezia Mestre, Italy.
Email: tofikahmed.shifa@unive.it, kassabelay.ibrahim@unive.it, alberto.vomiero@ltu.se and elisa.moretti@unive.it

Funding information
European Union's Horizon 2020, Marie Skłodowska-Curie, Grant/Award Number: 101027930; Italian Ministry of University and Research (MUR), Progetti di Ricerca di Rilevante Interesse Nazionale, PRIN 2022, Grant/Award Number: H53D23003840001; Kempe Foundation, Grant/Award Numbers: JCK1505, JCK1703, SMK1839

Abstract

The oxygen evolution reaction (OER) is a pivotal process in electrochemical energy conversion. Herein, we report a computational study-guided experimental work that uncovers the dynamics of active sites in a heterostructure composed of two distinct phases: Brunogeierite (Fe_2GeO_4) and serpentine ($Ni_3Ge_2O_5(OH)_4$). This heterostructure is synthesized by introducing varying amounts of a nickel precursor into pristine Fe_2GeO_4. When comparing pristine materials, Fe in Fe_2GeO_4 is better for OER as compared with the Ni in $Ni_3Ge_2O_5(OH)_4$. Interestingly, the Ni becomes more active in the heterostructure following the structural distortion and the induced increased electron transfer, which we proved by ex situ/in situ XAS studies. These findings highlight the dynamic evolution of active sites in the heterostructure, elucidating how the synergy between structural and electronic factors transforms catalytic behavior. The optimized heterostructure as an ideal model reveals enhanced electrocatalytic performance with an overpotential of 325 mV versus RHE to achieve a current density of 100 mA cm^{-2}, a Tafel slope of 42 mV dec^{-1}, and long-term stability

Tofik Ahmed Shifa, Karim Harrath, and Alhagie Jadama contributed equally.

exceeding 50 h even at high current densities, making it highly promising for a wide range of critical electrolysis applications.

KEYWORDS

active sites, electrochemical oxygen evolution, heterostructure, iron-nickel germanates

1 | INTRODUCTION

The oxygen evolution reaction (OER) is a vital cornerstone for assisting key cathodic processes: like the hydrogen evolution reaction (HER), carbon dioxide reduction reaction (CO_2RR), and nitrogen reduction reaction (NRR) paving the way for future renewable energy conversion and storage.[1] However, it remains a kinetically challenging process which demands highly efficient catalysts to overcome its sluggish reaction rates.[2] Currently, the state-of-the-art catalysts rely on noble metals such as Ir and Ru.[3] However, their limited availability on Earth and high costs impose constraints on their widespread application. There are also issues related to stability at higher anodic potentials.[4] Hence, there is significant pursuit for the development of materials with both high catalytic activity and cost-effectiveness, aiming to replace the currently leading noble-metal-based catalysts. Transition-metal-based compounds, including oxides, hydroxides, chalcogenides, and so on, have garnered widespread attention as catalysts for the OER due to their cost-effectiveness and abundant reserves.[5] Various approaches have been explored to improve the performance of these catalysts, with heterostructuring being particularly recognized and appreciated.[6] Heterostructures often manifest properties like structural disorder, defects, and multiple phases arising from lattice mismatch at the interface between different components. These properties, in turn, provide an increased number of catalytically active sites.[7] When heterostructures are systematically constructed using components from promising materials, the resulting interface typically exhibits synergistic effects, leading to overall outstanding performance. As to the promising materials, NiFe-based catalysts have been brought to the forefront due to their remarkable electrocatalytic performances.[8] Their status can be traced back to 1987, when Corrigan[9] demonstrated that introducing Fe at ultralow concentrations (0.01%) significantly enhanced the OER performance of nickel oxide. This pivotal finding accelerated the development of a wide variety of NiFe-based OER electrocatalysts. The nature of active sites in these materials remains an issue of debate.[10] Among the proposed locations are on Fe atoms,[11] on Ni atoms,[12] or synergy between Ni and Fe.[13] Generally, enhanced electrochemical performance is ascribed to improved structural flexibility and redox properties of active sites. Recent studies[14] suggest that incorporating redox-inert elements, such as germanium (Ge), can effectively modulate the electronic environment, thereby optimizing the adsorption energies of reaction intermediates and enhancing OER activity.

It is, therefore, reasonable to design a NiFe-based catalyst containing Ge as an integral part of the material. In this work, both DFT calculations and experimental corroborations were investigated to understand the active site evolution on the controllably synthesized Fe_2GeO_4–$Ni_3Ge_2O_5(OH)_4$ heterostructure. $Ni_3Ge_2O_5(OH)_4$ shows moderate adsorption energy on Ni sites. After integrating the Fe_2GeO_4, however, the adsorption energy on the Ni site dramatically decreased. We have corroborated this speculation by an XANES study to probe the evolution of active sites as we go from Fe_2GeO_4 to different materials by increasing Ni content till we get the optimized heterointerface Fe_2GeO–$Ni_3Ge_2O_5(OH)_4$. With these synergies, our catalyst exhibited robust performance as evidenced by the current densities of 10 and 100 mA cm^{-2} at overpotentials of 280 and 325 mV versus RHE, respectively. This study unveils the active sites' nature and the synergy between Fe and Ni atoms.

2 | RESULTS AND DISCUSSIONS

Computational studies were conducted aimed at understanding the mechanism underlying the promotional effect of the $Ni_3Ge_2O_5(OH)_4/Fe_2GeO_4$ heterostructure catalyst for the OER reaction. The Gibbs free energies of intermediates such as *OH, *O, and *OOH were calculated using DFT + U to understand the interactive effect of Fe and Ni atoms in the heterostructure. For comparison, we also considered isolated Fe_2GeO_4 and $Ni_3Ge_2O_5(OH)_4$ to highlight the role of heterostructure formation. The optimized structures of $Ni_3Ge_2O_5(OH)_4/Fe_2GeO_4$ (labeled as FeNiGeO-2), Fe_2GeO_4, and $Ni_3Ge_2O_5(OH)_4$ used in this study are shown in Figures 1A and S1a,b, respectively.

For OER catalysis, it is crucial to understand the effect of the heterostructure on the adsorption of *OH reactants, which could describe the catalyst metal sites' affinity to oxygen atoms. Due to the diversity of Fe sites

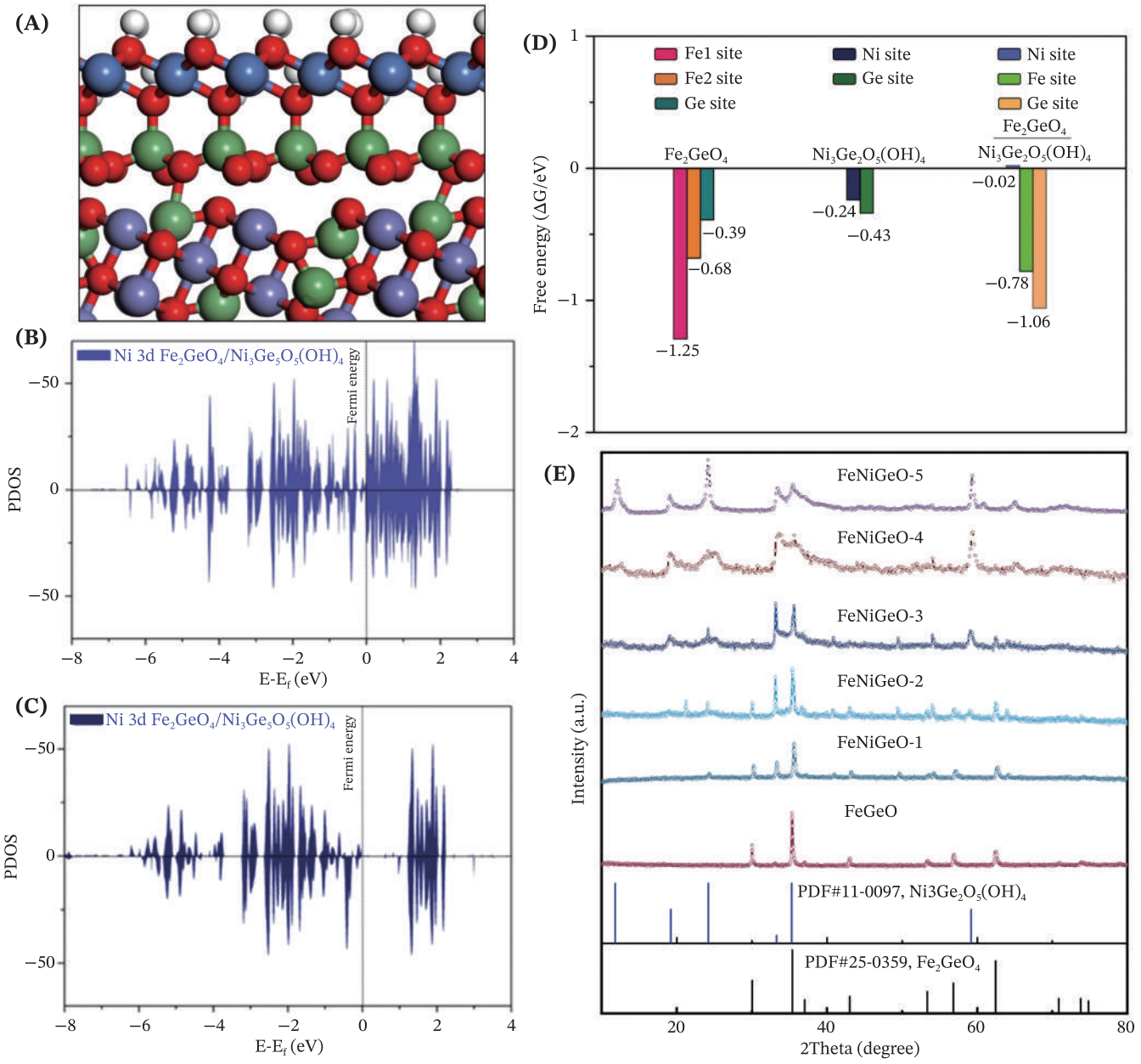

FIGURE 1 (A) The optimized structure of FeNiGeO-2, Fe = purple; Ni = blue; Ge = green; O = red. (B) The partial density of states (PDOS) for Ni in pristine $Ni_3Ge_2O_5(OH)_4$ and FeNiGeO-2. (C) The *OH adsorption profile at different sites on pristine materials and that of FeNiGeO-2. (D) The XRD patterns of the synthesized material in the Fe_2GeO_4 to $Ni_3Ge_2O_5(OH)_4$ series, with increasing content of nickel precursor addition (E).

in Fe_2GeO_4, we distinguished two different Fe sites at different oxidation states: Fe1, bound to three oxygen atoms, and Fe2, bound to four oxygen atoms. The results, illustrated in Figure 1B, show that the pristine Fe_2GeO_4 catalyst favors the adsorption of hydroxyl groups (OH) with adsorption energies of approximately −1.25 eV at the Fe1 site and −0.68 eV at the Fe2 site, while the adsorption energy for OH– is weaker at −0.39 eV on the Ge site. For the $Ni_3Ge_2O_5(OH)_4$ catalyst, OH is moderately adsorbed on the Ni site with an energy of −0.24 eV, and energy of −0.43 eV on Ge site. For the $Ni_3Ge_2O_5(OH)_4/Fe_2GeO_4$ heterostructure, the adsorption energies of OH are significantly increased, with values of −1.06 and −0.78 eV at the Fe2 and Ge sites, respectively, at the interface. This indicates a high affinity for adsorbing oxygenated intermediates, leading to a challenging transformation to O_2 product. Meanwhile, the adsorption of OH on the Ni site becomes weaker, with a positive energy of 0.02 eV, making it a potentially promising site for the OER reaction.

To understand the origin of this moderated adsorption energy, particularly at the Ni site in the heterostructure compared with the pristine $Ni_3Ge_2O_5(OH)_4$, we investigated

the electron flow at the interface. The partial density of states (PDOS) of nickel in both isolated $Ni_3Ge_2O_5(OH)_4$ and the heterostructure indicates metallic characteristics conducive to rapid electron transfer (Figure 1C,D). The PDOS for nickel at the interface surpasses that of isolated $Ni_3Ge_2O_5(OH)_4$ and the Fe2 site in Fe_2GeO_4 (Figure S1c) accompanied by an increase in density of states around the Fermi level. This shift enhances the electronic properties of the Ni active site, optimizing the oxygenate intermediate adsorption and rendering the $Ni_3Ge_2O_5(OH)_4/Fe_2GeO_4$ a catalyst with remarkable catalytic ability.

Guided by DFT insights, we synthesized Fe_2GeO_4 using a hydrothermal method and incrementally introduced varying amounts of a nickel precursor during the synthesis (details reported in the experimental section). This approach allowed us to systematically understand the effect of the material composition, ultimately achieving the optimized heterostructure.

The x-ray powder diffraction (XRD) was performed to confirm the crystal structure of the pristine Fe_2GeO_4 and the evolution, along with the addition of nickel precursor. As revealed in Figure 1E, the peaks representing diffraction patterns have a direct correlation to the pure phase of the reference material (PDF no. 25-0359). The sharp and well-defined nature of the peaks demonstrates the pure crystalline phase of cubic Brunogeierite. It adopts the spinel structure, typical for materials in the A_2BO_4 family, where the cations occupy specific tetrahedral (A) and octahedral (B) sites. In the spinel structure, Fe^{2+} ions typically occupy tetrahedral sites, and Ge^{4+} ions occupy octahedral sites. The oxygen ions form a close-packed arrangement, stabilizing the structure.[15] As this material undergoes incremental addition of nickel, the appearance of additional peaks is apparent, indicating a structural transition to a different phase. The increment is described as: FeGeO → FeNiGeO-1 → FeNiGeO-2 → FeNiGeO-3 → FeNiGeO-4 → FeNiGeO-5, where FeGeO represents the pristine Fe_2GeO_4 Brunogeierite phase and the FeNiGeO-5 represents the final $Ni_3Ge_2O_5(OH)_4$ serpentine phase, where a non-negligible fraction of the Fe_2GeO_4 Brunogeierite phase is still present. This trend evidences the existence of Brunogeierite phase (at the very beginning), then the formation of heterostructure with serpentine ($Fe_2GeO_4/Ni_3Ge_2O_5(OH)_4$) and eventually serpentine (Ni3Ge2O5(OH)4—PDF no. 11-0097) with a residual Brunogeierite phase at the other end. The optimized heterostructure, based on the DFT calculation, is therefore FeNiGeO-2. The morphology of the synthesized catalysts was observed using field emission scanning electron microscopy (FE-SEM). The SEM image of pure FeGeO exhibits polyhedral structures with distinct corners. With the incremental addition of nickel precursor, new morphology has become evident that can be attributed to layered $Ni_3Ge_2O_5(OH)_4$ nanosheets in addition to the polyhedron of FeGeO (Figure S2). This is further evidenced by the transmission electron microscope (TEM) images in Figure 2A,D. The well-faceted regular shape of the structures suggests well-formed crystallites with a high degree of crystallinity. This is strongly supported by the selected area electron diffraction (SAED) pattern. Figure 2B displays the pattern of a polycrystalline structure, due to the aggregation of many crystallites of different dimensions and orientations.

It is possible to recognize the typical d-spacings of Brunogeiete phase (Fe_2GeO_4) for the FeGeO sample, in accordance with the XRD results. High-resolution micrographs allow a deeper analysis of the nanometric platelets. In Figure 2C, d-spacings of 0.25 and 0.29 nm can be easily observed through the aid of Fourier transform (FFT). These crystal fringes highlighted in the FFT inserts can be attributed to a Brunogeiete phase of Fe_2GeO_4, as already seen in the SAED analysis. In the FeNiGeO-2 sample, the nano sheets become evident as seen from the TEM image in Figure 2D. The SAED data in Figure 2E displays a pattern of a polycrystalline structure that perfectly matches with that of FeGeO as in the case of the bigger square particles. In addition to this observation, it is possible to notice the presence of the 0.46 nm spot that does not belong to the Fe_2GeO_4 phase. This new spot can be attributed to a phase representing the (1 0 5) plane of the $Ni_3Ge_2O_5(OH)_4$. Moreover, the 0.46 nm spot is also evident from the HRTEM image of Figure 2F further confirming the advent of a new phase because of the controlled addition of nickel precursor. Figure 3 exhibits a high-angle annular dark-field scanning transmission electron microscopy (HAADF-STEM) image of FeNiGeO-2 composite. The energy dispersive x-ray spectroscopy (EDS) elemental mapping, displayed below the STEM micrograph in the figure, demonstrates a homogeneous distribution of Fe, Ge, O, and Ni within the composites. The EDS-STEM elemental mapping for FeGeO and the elemental analysis spectra for both pristine and the composite are presented in Figures S3 and S4, respectively, illustrating the presence of the elements with the desired stoichiometry.

Beyond confirming the presence of the elements, it is essential to understand their chemical valence states/electronic properties and how the incorporation of nickel influences these states. This understanding is critical, as the elemental states directly impact the dynamics of active sites and their effectiveness in OER catalysis. To this end, x-ray photoelectron spectroscopy (XPS) and x-ray absorption spectroscopy (XAS), including Fe and Ni K-edge x-ray absorption near-edge structure (XANES) and extended x-ray absorption fine structure (EXAFS), were employed to study the valence states and to

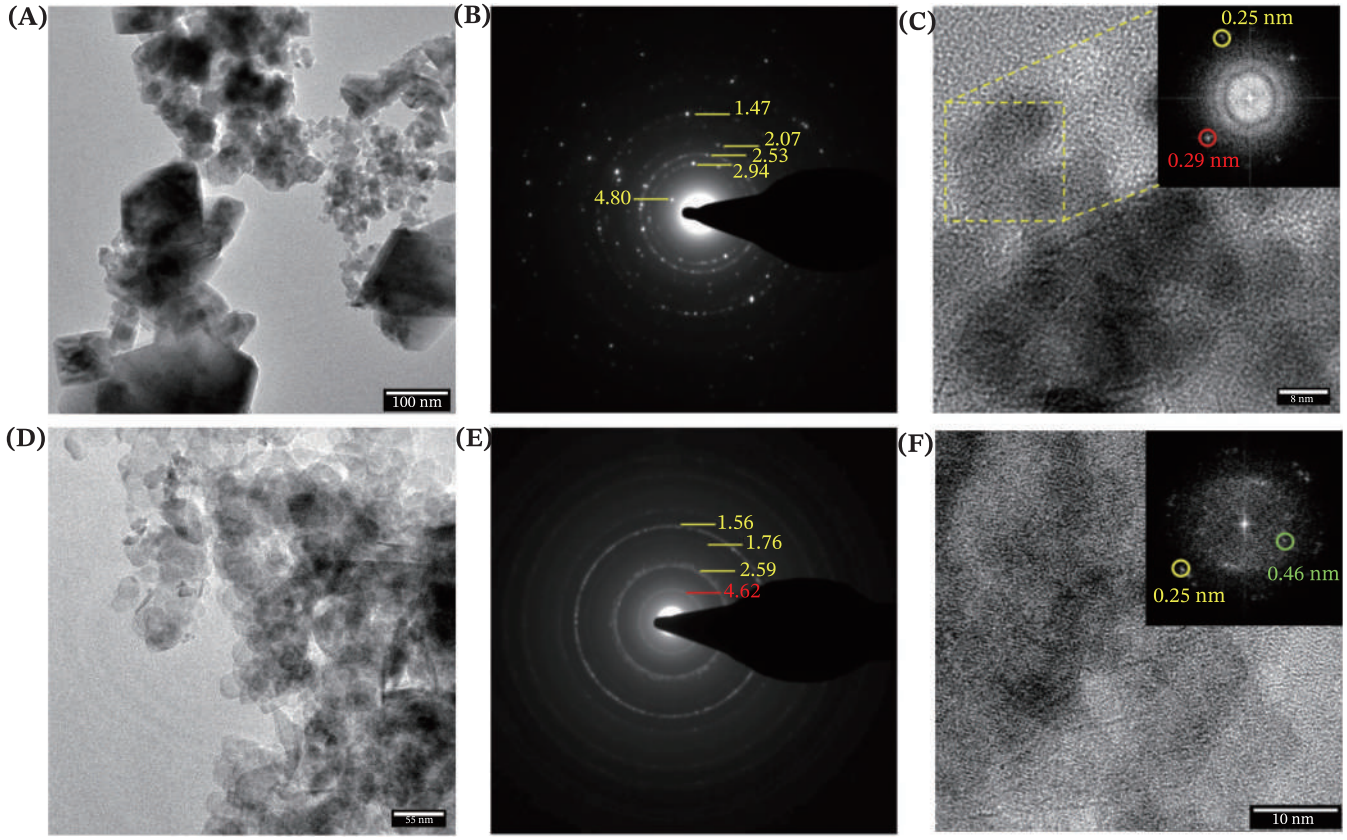

FIGURE 2 TEM image, SAED pattern and HRTEM image of FeGeO (A–C) and FeNiGeO-2 (D–F).

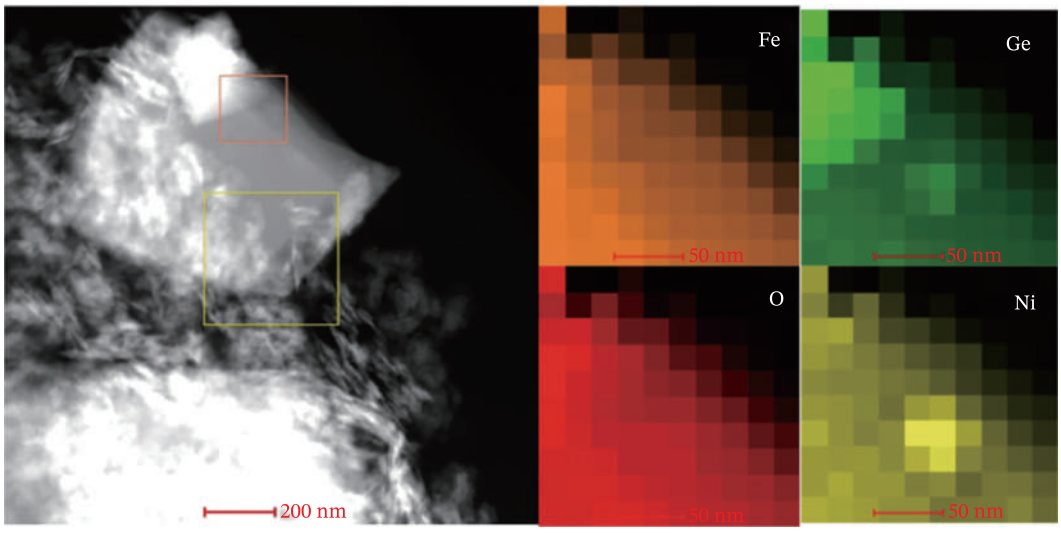

FIGURE 3 STEM-EDS elemental mapping for FeNiGeO-2.

understand the local atomic configurations within the catalysts. The deconvoluted Ni 3p XPS spectrum of FeNiGeO-2 in Figure S5 exhibits two distinct binding energies at 69.8 and 68.8 eV, corresponding to Ni^{2+} and a partially oxidized or hydroxylated Ni species, respectively.[16] The Fe 3p XPS spectra reveal distinct differences between FeGeO and FeNiGeO-2. In FeGeO, Fe exhibits a dominant sharp peak centered at ~56.2 eV, consistent with the Fe^{2+} oxidation state,[17] accompanied by a weaker shoulder at higher binding energy, which can be attributed to a satellite peak. In FeNiGeO-2, the Fe 3p peak broadens and shifts to ~56.8 eV, with satellite features

appearing at higher binding energies. This broadening and the presence of higher binding energy features suggest the coexistence of Fe^{2+} and Fe^{3+} oxidation states likely due to electronic interaction with Ni at the heterointerface. The Ge 3d spectra provide a much more straightforward picture of the chemical changes occurring as a result of the formation of a heterostructure between Fe2GeO4 and $Ni_3Ge_2O_5(OH)_4$. In FeGeO, a sharp peak at ~32 eV indicates that Ge exists predominantly as Ge^{4+} as in the spinel structure of Fe_2GeO_4.[18] In contrast, FeNiGeO-2 displays a broader Ge 3d region with multiple components which can be attributed to partially reduced or hydroxylated Ge species due to the formation of $Ni_3Ge_2O_5(OH)_4$ in addition to Fe_2GeO_4. The O 1s XPS spectra reveal a clear upshift in binding energy upon formation of the FeNiGeO-2 heterostructure. In pristine FeGeO, the spectrum is dominated by a peak at ~530.0 eV, attributed to lattice oxygen (O^{2-}) in Fe–O and Ge–O bonds, along with a shoulder at ~532.0 eV corresponding to surface hydroxyl species. In contrast, FeNiGeO-2 exhibits broader and higher binding energy features centered around ~531.6, 533.0, and ~535.0 eV, indicating a significantly more hydroxylated and disordered surface.[19] XANES and EXAFS provide further information that supports the presence of interfacial charge redistribution and altered local coordination environments induced by the introduction of Ni into the FeGeO matrix. Figure 4A shows the XANES spectra for the Fe K edge in the synthesized samples together with standard iron-containing materials used as references to assess the oxidation state of Fe in the synthesized materials. The comparison against the standard materials reveals that the oxidation state of Fe is found between 2+ and 4+. The other critical information would be about the effect of adding an increasing amount of Ni into FeGeO. The Fe K-edge shifts to higher energy as the concentration of Ni increases, suggesting that Fe loses an electron towards Ni. This observation can be corroborated from

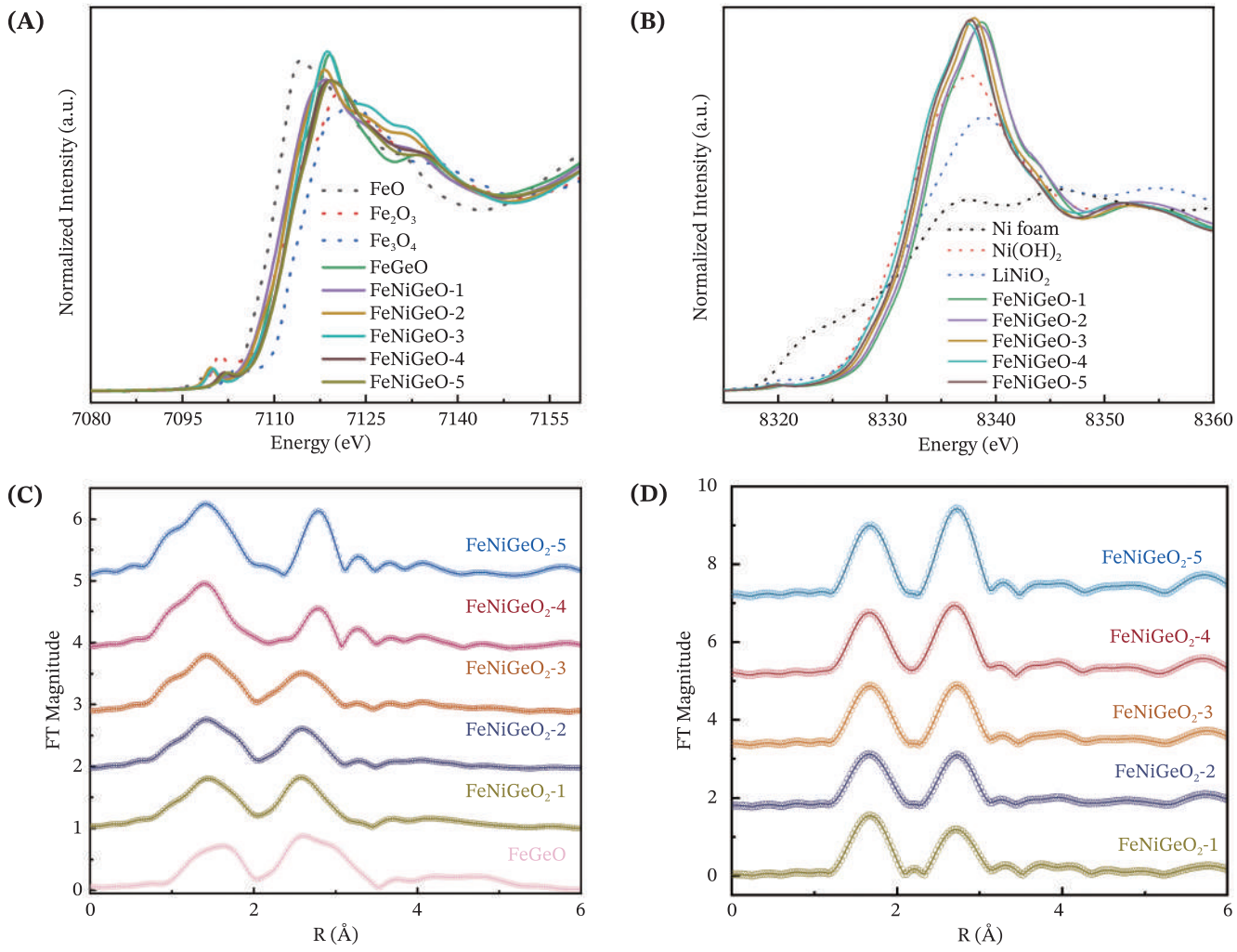

FIGURE 4 XANES spectra at Fe K-edge (A) and Ni K edge (B) of all the samples, together with the standard materials for comparison. (C) Fourier-transform EXAFS spectra from A. (D) Fourier-transform EXAFS spectra from B.

Figure 4B, which shows the XANES spectra of Ni-K edge where it shifts to lower energy, confirming that Ni gains electrons from Fe.

The local coordination environment results are presented in Figure 4C,D through the Fourier-transformed extended x-ray absorption fine structure (FT-EXAFS) spectra. The bond lengths for Fe–O and Fe–M interactions exhibit a shift to higher R values, particularly at higher Ni concentrations, indicating increased bond distortion. This can be rationalized by the fact that the insertion of Ni may alter bond angles and lengths, leading to larger average bond lengths due to structural adjustments. Notably, the intensity of the Fe–O bonding peak increases with the addition of Ni, suggesting that there is no associated non-metal vacancy (in this case oxygen). In contrast, the Fe–M bonding peak shows a decrease in intensity as Ni content rises, implying a reduction in the coordination number at the metal site, which could be attributed to the formation of Fe vacancies.

When it comes to the Ni K-edge EXAFS, the first peak around 1.6 Å belongs to Ni–O bonding and the 2nd peak at 2.7 Å belongs to Ni–M (M = Ni, Fe, or Ge). Figure 4D shows an increase in the intensity of these peaks with an increase in Ni content, confirming the increase in coordination number around Ni. However, both peaks show a shift to a lower *R* value, suggesting the local environment around Ni is shrinking. From the XAS study, it appears conclusive that the controlled addition of Ni into FeGeO induces significant structural and electronic modifications, leading to the formation of Fe vacancies. These vacancies, coupled with enhanced electronic interactions between Fe and Ni, promote optimal active sites for OER by facilitating charge transfer and improving oxygen adsorption kinetics. The synergistic effects of Ni incorporation and Fe vacancies underscore the potential of this doped system as a highly efficient electrocatalyst for water oxidation.

The FeNiGeO-2 and the other control samples were deposited on nickel foam (NF) substrate to probe the electrocatalytic performances towards OER in 1 M KOH. All the data were recorded in a standard three-electrode electrochemical cell using the synthesized sample/NF as the working electrode, an Ag/AgCl (3 M KCl) as the reference electrode, and a graphite rod as the counter electrode. Potentials obtained in this study were all calibrated to the reversible hydrogen electrode (RHE) reference for comparison (see Section 4 for details). Figure 5A shows the current and resistance (iR) corrected polarization curves presented as linear sweep voltammetry (LSV). It is apparent from the figure that the bare nickel foam exhibits negligible OER activity within the measured potential range, indicating that it does not contribute significantly to the overall catalytic performance.

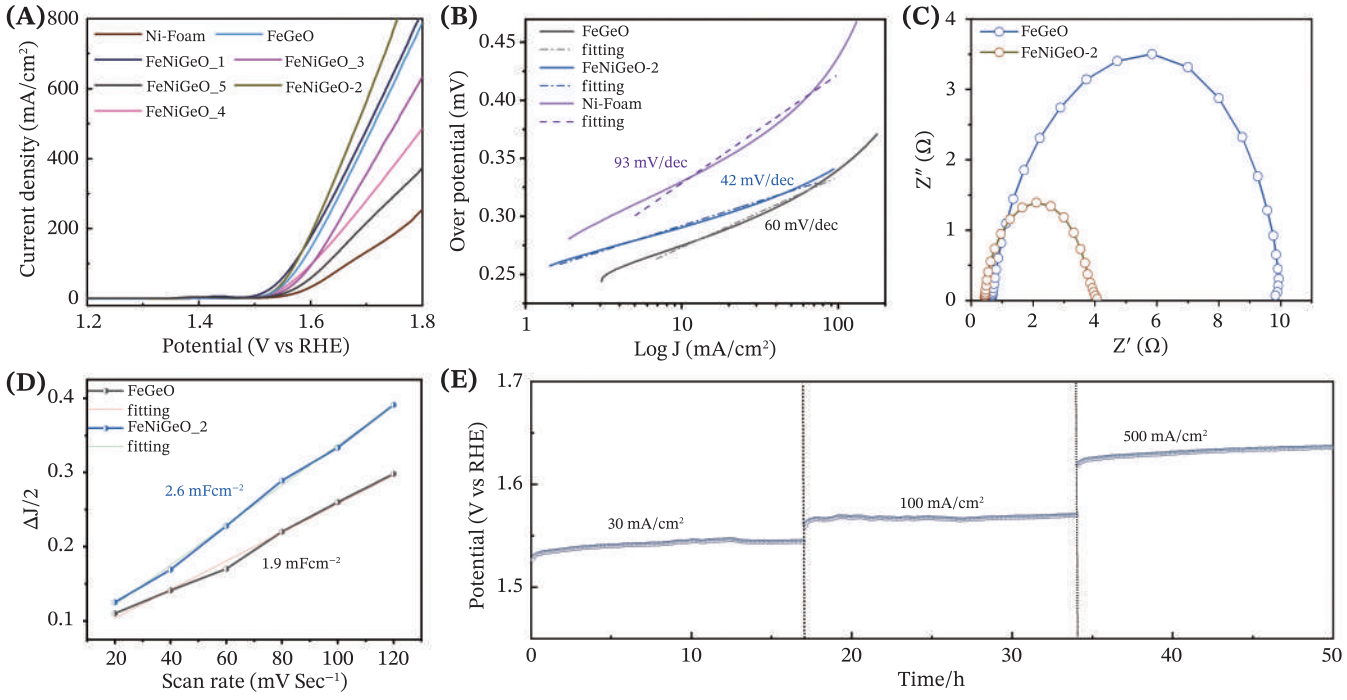

FIGURE 5 (A) Linear sweep voltammetry (LSV) curves. (B) Tafel plots extracted from the LSV curves in A. (C) Comparison of Nyquist plots for the FeGeO versus FeNiGeO-2. (D) Double-layer capacitance (Cdl) measurements of FeGeO and FeNiGeO-2. (E) Chronopotentiometric tests of the FeNiGeO-2 catalyst at a constant current densities of 30, 100, and 500 mA cm^{-2}.

This confirms that the observed activity for our synthesized samples arises from the active materials deposited on the nickel foam, not from the substrate itself. Accordingly, the electrocatalytic activity of FeNiGeO-2 is shown to have the best performance overall. It only requires an OER overpotential of 325 mV versus RHE to achieve a current density of 100 mA cm^{-2}, lower than the pristine FeGeO (350 mV vs. RHE) and other samples that have varied amounts of Ni. For further analysis on the electrocatalytic activity, Tafel slope was obtained from the corresponding LSV curves as shown in Figure 5B, where the lowest value (42 mV dec^{-1}) is recorded again for the FeNiGeO-2, indicating a favorable OER kinetics on its surface. This performance notably surpasses that of the other catalysts in this study and compares well with many recently reported non-precious metal-based electrocatalysts (Table S1). The Nyquist plot from the electrochemical impedance spectroscopy (EIS) reveals the smaller semicircles for this sample compared with the pristine FeGeO under the same conditions (Figure 5C), indicating that the optimum heterointerface causes the charge redistribution, thus lowering charge-transfer resistance. To further elucidate the electronic origin of this reduced resistance, we performed Mott–Schottky analysis (Figure S6). The negative slopes of the plots for both FeGeO and FeNiGeO-2 confirm their p-type semiconductor nature. Notably, the slope for the FeNiGeO-2 heterostructure is smaller in magnitude than that of pure FeGeO. According to the Mott–Schottky equation, this demonstrates a substantially higher density of charge carriers in the heterostructure.

We evaluated the catalysts' electrochemically active surface area (ECSA) by determining the double-layer capacitance (Cdl), which provides an estimate of the electrochemically exposed active sites. To do this, cyclic voltammetry measurements were conducted in the non-faradaic region at various scan rates (Figure S7). The differences in current densities as a function of scan rate were then calculated and plotted in Figure 5D. The Cdl value of FeNiGeO-2 (2.6 mF cm^{-2}) is found to be higher than that of FeGeO (1.9 mF cm^{-2}). This result may suggest that the heterointerface could have facilitated the increased exposure of active sites on the surface. Yet, there is no pronounced difference in this finding suggestive of the fact that the superior performance of FeNiGeO-2 likely stems from its enhanced intrinsic activity, conductivity, or favorable surface properties, rather than a significant difference in electrochemically active surface area. Analogous reports have recently been communicated.[20] Electrochemical durability is another key index to evaluate the performance of the electrocatalysts, as it addresses a significant bottleneck in achieving scalable water-splitting technology. This parameter was evaluated via chronopotentiometry test at the current densities of 30, 100, and 500 mA cm^{-2}. As plotted in Figure 4E, the catalyst exhibits a stable performance for about 50 h of continues operation.

To gain in-depth insights into the dynamics of active sites and the electrocatalytic mechanism during the OER process, two routes were pursued: (i) In situ XANES measurements (Figure 6A) were conducted at both the Ni K-edge and the Fe K edge from open circuit voltage (OCV) to 1.55 V versus RHE in 1 M KOH, providing real-time information on the electronic and structural changes of the catalyst under operating conditions. (ii) Further DFT calculations were performed on the optimized surface to elucidate the reaction pathways and the energetics of the intermediate species. Both approaches provided profound insights into the nature of the active sites and their evolution during the OER process, offering valuable clues about the underlying catalytic mechanism and the key factors contributing to the enhanced activity.

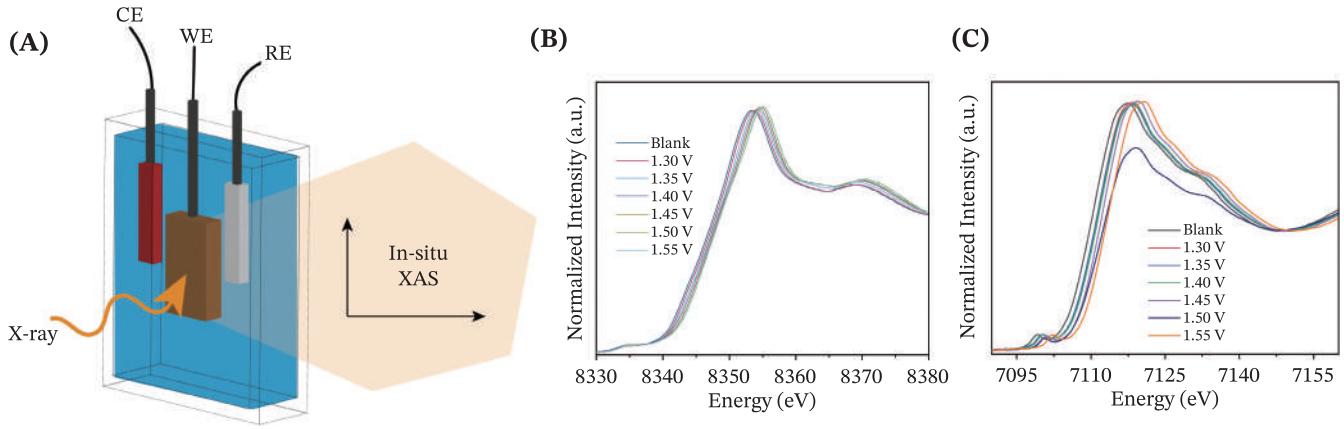

FIGURE 6 (A) A schematic depicting the in-situ XANES measurements. In situ XANES spectra collected at various voltages starting from the OCV at Ni K edge (B) and Fe K edge (C) on FeNiGeO-2 sample.

Accordingly, Figure 6B shows the in situ XANES spectra of the Ni K edge with a clear positive shift in the main edge position observed as the applied potential increases from 1.30 to 1.55 V. This shift indicates the progressive oxidation of Ni species, suggesting their involvement in the OER process. The Ni species may undergo a transition from lower oxidation states to higher oxidation states under applied potential.

A similar trend in edge shift is observed for the Fe K-edge (Figure 6C), indicating changes in the oxidation state of Fe as the applied potential increases. The observed positive shifts in Ni and Fe K-edges with increasing potential are consistent with the formation of high-valent Ni^{3+}/Ni^{4+} and Fe^{3+}/Fe^{4+} species, suggesting cooperative interaction between Ni and Fe during the OER process. Thus, the active sites are likely mixed-valence Ni and Fe species formed in situ under the applied potential, with Ni possibly serving as the primary active site and Fe enhancing activity through electronic modulation or direct participation. Further insight could be collected from the DFT calculations. As to the findings from the DFT calculations, we investigated the charge difference density and density of states to gain insights into electron transfer dynamics at the $Ni_3Ge_2O_5(OH)_4/Fe_2GeO_4$ interface. As depicted in Figure 7A, electron redistribution at the interface indicates a discernible electron flow from Fe_2GeO_4 to $Ni_3Ge_2O_5(OH)_4$, corroborated by XAS results.

The Gibbs free energy related to the OER reaction pathways and the model structures on the isolated Fe_2GeO_4 and $Ni_3Ge_2O_5(OH)_4$ materials are summarized in Figures S8 and S9, respectively. The free energy values for different intermediate steps reveal that the dehydrogenation of the *OOH intermediate to form the O_2 product is the rate-determining step (RDS), with energy changes of 1.38 and 1.00 V for the Fe1 and Fe2 sites, respectively, while the Ge site exhibits an energy of 1.31 V for the deprotonation of *OH to form the *O intermediate. For the $Ni_3Ge_2O_5(OH)_4$ catalyst, both the Ni and Ge sites exhibit similar activities, with the potential determining step (PDS) corresponding to the transformation of *OH to *O, with energies of about 1.23 and 1.17 V, respectively. These results suggest that Fe_2GeO_4 could provide better OER activity since the Fe2 site presents a lower

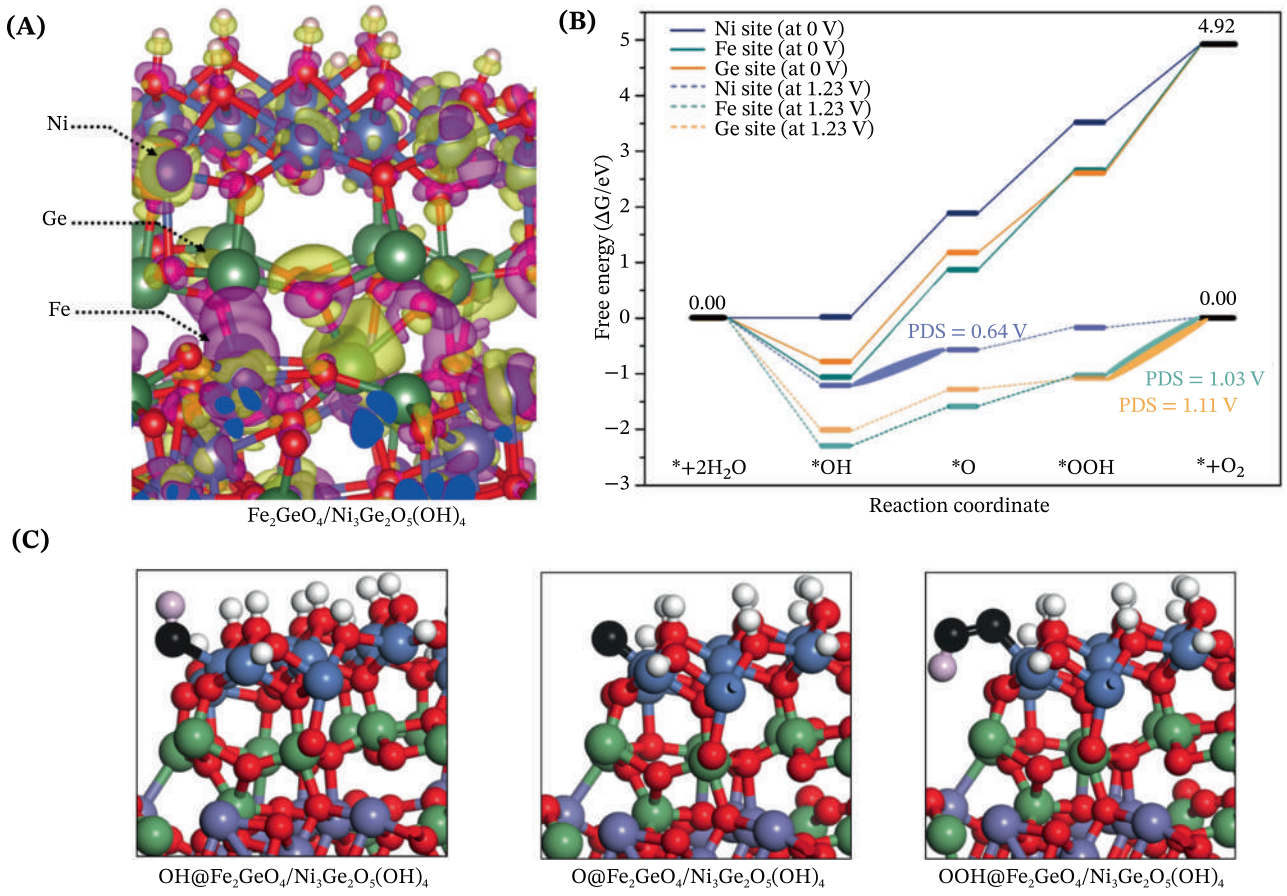

FIGURE 7 (A) Charge density differences of $Fe_2GeO_4/Ni_3Ge_5O_5(OH)_4$, (B) OER free energy profile on different sites on $Fe_2GeO_4/Ni_3Ge_5O_5(OH)_4$ and (C) structure of OER intermediates on $Fe_2GeO_4/Ni_3Ge_5O_5(OH)_4$ at Ni site.

PDS compared with the Ni or Ge sites in $Ni_3Ge_2O_5(OH)_4$. This could be explained by the higher density of states around the Fermi level for the Fe site in Fe_2GeO_4 compared with the Ni site in $Ni_3Ge_2O_5(OH)_4$. For the $Ni_3Ge_2O_5(OH)_4/Fe_2GeO_4$ heterostructure model, the OER free energy profile presented in Figure 7B shows enhanced Ni site activity, with a significant decrease in PDS to 0.64 V. The limiting step corresponds to the dehydrogenation of the *OH intermediate to form the *O intermediate. Figure 7C illustrates the adsorption of intermediates (*OH, *O, and *OOH) on the surface of the FeNiGeO-2 heterostructure, providing a clear visualization of the active sites and offering insight into how the intermediates interact with and bind to the surface (schematically summarized in Figure S10). These results align with/solidify experimental findings, indicating that the Ni site is the main site responsible for the OER activity.

3 | CONCLUSIONS

In summary, guided by computational study, we synthesized a series of materials starting from Fe_2GeO_4 with increasing concentrations of Ni to get the optimized heterostructure as an efficient electrocatalyst for driving the OER in alkaline solutions. The heterostructure combines Fe_2GeO_4 and $Ni_3Ge_2O_5(OH)_4$, two phases with complementary properties improving the kinetics of the OER by facilitating intermediates adsorption and dissociation. The insertion of Ni enhances the catalytic activity by modifying the electronic structure of Fe at the interface. Ni sites often act as the main adsorption centers for OER intermediates, while Fe assists in tuning the electronic environment, leading to a lower overpotential. This work offers valuable insights into the nature of active sites in catalysts containing both Ni and Fe within two distinct crystal phases, guiding the development of efficient and stable catalysts toward water oxidation and other heterogeneous catalysis.

4 | EXPERIMENTAL METHODS

4.1 | Synthesis of the catalysts

The Fe_2GeO_4 polyhedrons were synthesized using hydrothermal methods. Typically, 1.2 g (6 mmol) of $FeCl_2 \cdot 4H_2O$ was dissolved in 20 mL of DI water in a flask. This was then followed by dispersing 0.2 g of GeO_2 (2 mmol) in 20 mL of DI water with the subsequent addition of NaOH (0.6 g, 15 mmol) to the GeO_2 solution under magnetic stirring. The two solutions ($FeCl_2 \cdot 4H_2O$ (aq) and GeO2 (aq)) were mixed and stirred for 30 min at room temperature before being transferred into a Teflon-lined stainless-steel autoclave. The reaction solution was then maintained at 180°C for 24 h in a muffle furnace and later cooled down to room temperature before being collected and rinsed several times using DI water and ethanol via centrifugation. The samples were dried at 80°C overnight in an oven and later collected for further characterization analyses. The obtained product was denoted as FeGeO. The rest of the samples were synthesized similarly, but adding a weighed amount of $Ni(NO_3)_2 \cdot 6H_2O$ at the expense of $FeCl_2 \cdot 4H_2O$ and named as follows according to their concentration of Ni: FeNiGeO-1 (∼1% Ni), FeNiGeO-2 (∼3% Ni), FeNiGeO-3 (∼5% Ni), FeNiGeO-4 (∼18% Ni), and FeNiGeO-5 (∼25% Ni).

4.2 | Characterizations

Field-emission scanning electron microscopy (FESEM), Magellan XHR 400 L with a 10 kV electron beam was used to investigate the morphology of the as-synthesized samples. Further detail on the morphology, crystal structure, and composition was obtained from the FEI Tecnai F20 high-resolution transmission electron microscope (HRTEM), equipped with a Schottky emitter operating at 200 kV. Elemental analysis was performed by energy-dispersive x-ray spectroscopy (EDS), coupled to scanning transmission electron microscopy (STEM-HAADF) to map elemental distribution. An x-ray diffractogram was obtained from the PanAnalytical Empyrean XRD using Cu $k\alpha$ radiation. XANES and EXAFS spectra at the Ni K-edge and Fe K-edge were recorded in transmission mode at the XAFS experimental end station of the synchrotron Elettra by mounting the sample (as pellets) on a sample holder using Kapton tape in a vacuum chamber. The Si (1 1 1) fixed-exit double crystal monochromator of 1.4×10^{-4} resolving power was calibrated to the first-derivative maximum of the K-edge absorption spectrum of a metallic Fe foil (7112.0 eV) and it was detuned to exclude higher order harmonics. The Athena software package was used to analyze the data.

4.3 | Electrochemical measurements

A typical three-electrode system (reference electrode: Ag/AgCl, counter electrode: graphite rod and working electrode: the synthesized novel material) was used to assess the OER performances of the synthesized materials. To prepare the catalyst ink, the catalyst powder (4 mg) and carbon black (1 mg) were ground thoroughly and dispersed in a mixed solution of isopropanol (450 µL), DI water (50 µL), and 5 wt% Nafion (20 µL). The catalytic ink (10 µL) was then uniformly deposited on 0.5×0.5 cm Ni foam. A biologic electrochemical

workstation was used to evaluate the OER properties of all the catalysts in KOH (1 M) electrolytes. All potentials measured were calibrated to RHE using the following equation: ERHE = EAg/AgCl + 0.197 V + 0.059 pH. OER polarization curves were recorded at a scan rate of 5 mV s^{-1}. Before recording, the potential of the working electrode was scanned for five cycles until a stable cyclic voltammogram was recorded. Charge transfer resistance (Rct) was obtained using electrochemical impedance spectroscopy (EIS) measurements, applying an alternating current (AC) voltage (5 mV amplitude) over a frequency range of 100 kHz to 0.1 Hz. The electrochemical double-layer capacitance, which is expected to be linearly proportional to the ECSA, was determined by measuring the capacitive current at the non-Faradic region from scan rate-dependent CV runs. To perform the durability test, chronopotentiometry was run in 1.0 M KOH electrolyte at room temperature with current densities of 30, 100, and 500 mA cm^{-2}.

4.4 | DFT calculation methods

The spin-polarized DFT calculations with the Perdew–Burke–Ernzerhof (PBE) exchange-correlation functional[21] were performed using the Vienna ab initio simulation package (VASP).[22] The projector augmented wave method (PAW)[23] with a plane-wave kinetic energy cutoff of 500 eV was used, with the Gaussian smearing of 0.05 eV. The Hubbard correction of DFT + U is applied for Fe and Ni atoms with a value of 3 and 5.3 eV, respectively.[24] The Brillouin zone was sampled by 3 × 3 × 1 K-point for geometry optimization and 6 × 6 × 1 K-point to calculate the DOS calculations. The Fe_2GeO_4 (311) surface was modeled by a (1 × 1) supercell, and a (3 × 3) supercell modeled the $Ni_3Ge_2O_5(OH)_4$ (001) surface, and then both surfaces were used for build the $Ni_3Ge_2O_5(OH)_4/Fe_2GeO_4$ heterostructure. We have added a vacuum layer of 15 Å in all models to avoid periodic interactions All atoms were allowed to relax during geometry optimization, and the atomic positions were optimized till the forces were <0.03 eV $Å^{-1}$. The lattice dimensions were optimized simultaneously with the geometry. The structure of isolated molecules (O_2, H_2, and H_2O) was optimized within a unit cell measuring 15 Å × 15 Å × 15 Å, with only the Γ-point utilized.[25] The effects of van der Waals corrections were modeled using Grimme's method, with Becke–Jonson damping.[26] The binding energy of the OH is defined as the following equation: $E^{OH}_{binding} = E_{total} - E_{surafce} - EOH$, where $E_{surafce}$ is the energy of the Fe_2GeO_4, $Ni_3Ge_2O_5(OH)_4$ or $Ni_3Ge_2O_5(OH)_4/Fe_2GeO_4$ heterostructure. The EOH is calculated from following equation $EOH = EH_2O - 1/2EH_2$.

The Gibbs free energy of a species is calculated as the following equation:

$$G = E + \mathrm{ZPE} - TS,$$

where, E is the total energy of a species obtained from DFT calculations, ZPE and S are the zero-point energy and entropy of a species, respectively, and $T = 298.15$ K.

ACKNOWLEDGMENTS

This work was supported by the European Commission – Horizon 2020 (Marie Skłodowska-Curie Actions, 101027930) and the Ministero dell'Università e della Ricerca (MUR) under the PRIN 2022 programme (Progetti di Ricerca di Rilevante Interesse Nazionale), Project code: H53D23003840001. The authors would also like to thank the support by the Kempe Foundation (JCK1505, JCK1703, SMK1839).

CONFLICT OF INTEREST STATEMENT

The authors declare no conflict of interest.

DATA AVAILABILITY STATEMENT

The data that support the findings of this study are available on request from the corresponding author. The data are not publicly available due to privacy or ethical restrictions.

ORCID

Alberto Vomiero https://orcid.org/0000-0003-2935-1165

REFERENCES

1. (a) Stamenkovic VR, Strmcnik D, Lopes PP, Markovic NM. Energy and fuels from electrochemical interfaces. *Nat Mater*. 2017;161(1):57. (b) Wang J, Kim S-J, Liu J, et al. Redirecting dynamic surface restructuring of a layered transition metal oxide catalyst for superior water oxidation. *Nat Catal*. 2021;4(3):212.
2. (a) Wang X, Zhong H, Xi S, et al. Understanding of oxygen redox in the oxygen evolution reaction. *Adv Mater*. 2022;34(50): e2107956. (b) Boakye FO, Harrath K, Zhang D, et al. Synergistic engineering of dopant and support of Ru oxide catalyst enables ultrahigh performance for acidic oxygen evolution. *Adv Funct Mater*. 2024;34(48):2408714. (c) Qayum A, Harrath K, Li R, et al. Dynamically reconstructed Fe-CoOOH semi-crystalline electrocatalyst for efficient oxygen evolution reaction. *Small*. 2025;21:2408854. (e) Rafiq M, Harrath K, Feng M, et al. The XRD peaks of NMB can be indexed to Ni2B (JCPDS No. 48-1222). *Energy Mater*. 2024;14:2402866.
3. Mccrory CCL, Jung S, Peters JC, Jaramillo TF. Benchmarking heterogeneous electrocatalysts for the oxygen evolution reaction. *J Am Chem Soc*. 2013;135(45):16977-16987.
4. Kibsgaard J, Chorkendorff I. Considerations for the scaling-up of water splitting catalysts. *Nat Energy*. 2019;4(6):430-433.
5. (a) Ding H, Liu H, Chu W, Wu C, Xie Y. Structural transformation of heterogeneous materials for electrocatalytic oxygen

evolution reaction. *Chem Rev*. 2021;121(21):13174-13212. (b) Kim JS, Kim B, Kim H, Kang K. Recent Progress on multimetal oxide catalysts for the oxygen evolution reaction. *Adv Energy Mater*. 2018;8(11):1702774.

6. (a) Tofik A, Shifa, Wang F, Liu Y, He J. Heterostructures based on 2D materials: a versatile platform for efficient catalysis. *Adv Mater*. 2019;31:1804828. (b) Zhai P, Xia M, Wu Y, et al. Engineering single-atomic ruthenium catalytic sites on defective nickel-iron layered double hydroxide for overall water splitting. *Nat Commun*. 2021;12:4587.
7. (a) Xu Q, Zhang J, Zhang H, et al. Atomic heterointerface engineering overcomes the activity limitation of electrocatalysts and promises highly-efficient alkaline water splitting. *Energ Environ Sci*. 2021;14(10):5228-5259. (b) Shifa TA, Gradone A, Yusupov K, et al. Interfacing CrOx and CuS for synergistically enhanced water oxidation catalysis. *Chem Eng J*. 2023;453:139781.
8. (a) Dionigi F, Strasser P, Dionigi F, Strasser P. NiFe-based (oxy) hydroxide catalysts for oxygen evolution reaction in non-acidic electrolytes. *Adv Energy Mater*. 2016;6(23):1600621. (b) Ha MA, Alia SM, Norman AG, Miller EM. Fe-doped Ni-based catalysts surpass Ir-baselines for oxygen evolution due to optimal charge-transfer characteristics. *ACS Catal*. 2024;14(23):17347-17359.
9. Corrigan DA. The catalysis of the oxygen evolution reaction by iron impurities in thin film nickel oxide electrodes. *J Electrochem Soc*. 1987;134(2):377-384.
10. Magnier L, Cossard G, Martin V, et al. Fe–Ni-based alloys as highly active and low-cost oxygen evolution reaction catalyst in alkaline media. *Nat Mater*. 2024;23(2):252-261.
11. Friebel D, Louie MW, Bajdich M, et al. Identification of highly active Fe sites in (Ni,Fe)OOH for electrocatalytic water splitting. *J Am Chem Soc*. 2015;137(3):1305-1313.
12. Schä H, Sadaf S, Walder L, et al. Stainless steel made to rust: a robust water-splitting catalyst with benchmark characteristics. *Energy Environ Sci*. 2015;8:2685.
13. (a) Görlin M, Chernev P, De Araújo JF, et al. Oxygen evolution reaction dynamics, faradaic charge efficiency, and the active metal redox states of Ni–Fe oxide water splitting electrocatalysts. *J Am Chem Soc*. 2016;138(17):5603-5614. (b) Qiu Z, Tai CW, Niklasson GA, Edvinsson T. Direct observation of active catalyst surface phases and the effect of dynamic self-optimization in NiFe-layered double hydroxides for alkaline water splitting. *Energ Environ Sci*. 2019;12(2):572-581.
14. (a) Yoon KY, Park J, Jung M, et al. NiFeOx decorated Ge-hematite/perovskite for an efficient water splitting system. *Nat Commun*. 2021;12(1):4309. (b) Guo W, Luo H, Jiang Z, et al. Ge-doped cobalt oxide for electrocatalytic and photocatalytic water splitting. *ACS Catal*. 2022;12(19):12000-12013.
15. Setkova TV, Spivak AV, Borovikova EY, et al. Synthetic brunogeierite Fe_2GeO_4: XRD, Mössbauer and Raman high-pressure study. *Spectrochim Acta Part A Mol Biomol Spectrosc*. 2022;267(2):120597.
16. McBean CL, Liu H, Scofield ME, et al. Generalizable, electroless, template-assisted synthesis and electrocatalytic mechanistic understanding of perovskite $LaNiO_3$ nanorods as viable, supportless oxygen evolution reaction catalysts in alkaline media. *ACS Appl Mater Interfaces*. 2017;9(29):24634-24648.
17. Yamashita T, Hayes P. Analysis of XPS spectra of Fe^{2+} and Fe^{3+} ions in oxide materials. *Appl Surf Sci*. 2008;254(8):2441-2449.
18. Fredrick SJ, Prieto AL. Solution synthesis and reactivity of colloidal Fe_2GeS_4: a potential candidate for earth abundant, nanostructured photovoltaics. *J Am Chem Soc*. 2013;135(49):18256-18259.
19. Vukašinović J, Rapljenović Ž, Počuča-Nešić M, Ivek T, Branković Z, Branković G. The crucial role of defect structure in understanding the electrical properties of spark plasma sintered antimony doped barium stannate. *Mater Res Express*. 2023;10(1):15901.
20. (a) Sun N, Zheng Z, Lai Z, et al. Augmented electrochemical oxygen evolution by d-p orbital electron coupling. *Adv Mater*. 2024;36:2404772. (b) Yu F, Zhou H, Huang Y, et al. High-performance bifunctional porous non-noble metal phosphide catalyst for overall water splitting. *Nat Commun*. 2018;91(9):2551.
21. Perdew JP, Burke K, Ernzerhof M. Generalized gradient approximation made simple. *Phys Rev Lett*. 1996;77(18):3865-3868.
22. VASP. Vienna Ab initio Simulation Package. https://www.vasp.at/
23. (a) Joubert D. From ultrasoft pseudopotentials to the projector augmented-wave method. *Phys Rev B*. 1999;59(3):1758-1775. (b) Blöchl PE. Projector augmented-wave method. *Phys Rev B*. 1994;50(24):17953-17979.
24. (a) Harrath K, Yao Z, Jiang YF, Wang YG, Li J. Tailoring the active-site spacing of a single-atom catalyst for CH_4-to-CH_3OH conversion: the Co1/UiO-66 MOF as an exemplary model. *J Phys Chem C*. 2024;128(13):5579-5589. (b) Jiang S, Mushrif SH. Determining surface-specific Hubbard-Ucorrections and identifying key adsorbates on nickel and cobalt oxide catalyst surfaces. *Phys Chem Chem Phys*. 2023;25(12):8903-8912.
25. (a) Bahri L, Mbarki F, Harrath K. Understanding the direct methane conversion to oxygenates on graphene-supported single 3D metal atom catalysts. *Chem Pap*. 2023;77(7):3759-3767. (b) Harrath K, Yao Z, Jiang YF, Wang YG, Li J. Activity origin of the nickel cluster on TiC support for nonoxidative methane conversion. *J Phys Chem Lett*. 2023;14(17):4033-4041.
26. (a) Grimme S, Antony J, Ehrlich S, Krieg H. A consistent and accurateab initioparametrization of density functional dispersion correction (DFT-D) for the 94 elements H-Pu. *J Chem Phys*. 2010;132(15):154104. (b) Grimme S. Density functional theory with London dispersion corrections. *Wiley Interdiscip Rev Comput Mol Sci*. 2011;1(2):211.

SUPPORTING INFORMATION

Additional supporting information can be found online in the Supporting Information section at the end of this article.

How to cite this article: Shifa TA, Harrath K, Jadama A, et al. Exploring the evolution of active sites on Fe_2GeO_4–$Ni_3Ge_2O_5(OH)_4$ interfaces for water oxidation. *InfoMat*. 2025;7(12):e70073. doi:10.1002/inf2.70073